Title	Non-contact imaging for delamination using diffuse field concept
Author(s)	Nakao, Shogo; Hayashi, Takahiro
Citation	Japanese Journal of Applied Physics. 2019, 58, p. SGGB07
Version Type	AM
URL	https://hdl.handle.net/11094/84494
rights	© 2019 The Japan Society of Applied Physics. This Accepted Manuscript is available for reuse under a Creative Commons Attribution-NonCommercial-NoDerivatives 4.0 International License after the 12 month embargo period provided that all the terms of the license are adhered to.
Note	

Non-contact imaging for delamination using diffuse field concept

Shogo Nakao[1], and Takahiro Hayashi[1*]

[1]*Graduate School of Engineering, Department of Aeronautics and Astronautics, Kyoto University, Kyoto 615-8510, Japan.*

[*]E-mail: hayashi@kuaero.kyoto-u.ac.jp

The non-contact measurement called Scanning Laser Source (SLS) technique is applied to imaging inspection for subsurface delamination in a metal block and the effect of frequencies used for imaging is discussed with Finite Element Method (FEM) and experiments for an aluminum alloy block. First, FE formulation for the vibration of a closed structure described the relation between resonances in the whole structure and vibration distributions, and FE calculation provided the resonant frequencies and the resonant patterns of a metal block, which agreed well with experimental results. Next, images were obtained for a specimen with delamination using the SLS technique. When narrowband burst waves were used, the delamination images were largely different due to the resonances. For broadband chirp waves, the clear delamination images could be obtained in the frequency ranges including multiple resonant frequencies because diffuse fields were well established.

1. Introduction

Ultrasonic is widely used to inspect and evaluate such defects as degradation, cracks and delamination in engineering products. Generally, an ultrasonic transducer is attached to an inspected material through coupling agents such as water or gel for excitation and reception of elastic waves. However, such coupling agents are often unpreferable for final engineering products, and the use of ultrasonic transducers compels access to an inspected area even of large structures such as bridges and pipes. As an effective means for such applications, a non-contact and nondestructive evaluation (NDE) called laser ultrasonics has become widely used[1-8]. In the laser ultrasonics, giant pulses with the pulse duration of several dozen nanoseconds are emitted on the surface of a material to excite pulsed-elastic waves with the center frequency of a few MHz, and then vibrations are detected on the surface by a laser vibrometer using laser interferences. The noncontact measurements enable us to scan a laser spot and to detect vibrations at multiple positions for two-dimensional imaging.

However, vibration detection with a laser interferometer is often unstable under such bad conditions as fast scanning, remote measurements over 10 meters, and rough surfaces of inspected objects, because it requires precise measurements of interferences between scattering laser beam and reference laser beam. Therefore, the authors have studied NDE for defects in plate-like structures using Scanning Laser Source (SLS) technique in which a laser source is scanned and elastic waves are received at a fixed position[9-16]. The stable measurements through the SLS technique enabled us to create defect images even in curved structures such as a straight pipe and a branch pipe[9]. In addition, it was confirmed that clear images through the SLS technique can be obtained even using low frequency range[10]. For example, the SLS imaging for defects of the order of mm can be conducted using an audible frequency range below 15 kHz. Since such low frequency ranges can be used, we developed a measurement method in which MEMS microphones were used as a receiving device in Ref. 11).

The authors have also applied the SLS technique to adhesive bonding and delamination in plate-like structures[12, 13], which indicated that the SLS technique is effective even to create rough images of debonding and delamination. Moreover, we experimentally confirmed that clearer images can be obtained using the waves with wide frequency range such as chirp waves because the resonant frequencies of the entire structure severely affect

the images of debonding and delamination. Based on these results, Refs. 14) and 15) showed that diffuse field concept is effective for the defect imaging.

Unlike conventional NDE using coherent fields, the NDE using the diffuse field concept manages multiple reflections from the surfaces of a closed object. The diffuse field NDE is feasible even in a low frequency range with long wavelength that has not been used in the coherent field NDE due to the superposition of reflected waves, and the use of low frequency range generally facilitates the measurements. Conversely, small defects that have not been detected can be inspected in the frequency range measured with commercial receivers. Therefore, this study aims to clarify appropriate frequency ranges in the SLS imaging to inspect delamination using the diffuse field concept, and discusses applications to inspection for defects of the order of submillimeter.

2. The overview of the SLS imaging using diffuse field

The imaging technique using the SLS measurements utilizes flexural wave energy that varies with positions of the laser source. Figure 1 shows the principle of the SLS imaging in which elastic waves are received at a fixed position while scanning a laser source. If the thickness of a material near the laser source is thin due to degradation or wall thinning, then the energy of the flexural waves excited by laser irradiation becomes larger. Conversely, the energy of the flexural waves excited at an intact area becomes smaller. These tendencies indicate that the energy of flexural waves depends on the local bending stiffness of a material near the laser source. Therefore, images of internal defects and wall thinning can be obtained using the variations of flexural wave energy[9-16].

The authors have been trying to obtain images using burst waves and chirp waves generated with laser modulation, which revealed that the resonant patterns of an entire structure strongly appear in the images for burst waves and clearer images are created using chirp waves due to the reduction of the resonance patterns. It was proved that this effect is due to a diffuse field in the structure[15].

Diffuse field means a wave field with approximately homogeneous energy density in a whole structure as a result of multiple and random reflections. In order to establish diffuse fields appropriately, multiple resonant modes need to be superposed in a structure, and therefore the following three conditions should be required: waves with a wide frequency

3

range are needed, a structure must be closed for multiple reflections, and waves propagate with low viscous damping in the material and low leakage into surrounding media. If diffuse field is established in a structure, then the energy of vibration received at a certain time does not depend on the positions of exciting and receiving waves, and moreover, the energy of the received waves is proportional to that of the excited waves[19]. In the case of plate-like structures where an out-of-plane vibration is dominant, Weaver showed that the vibration energy in an entire structure is proportional to the power spectrum of an out-of-plane displacement [20]. This means that, once diffuse fields are established, the information of wave sources can be obtained with the measurement of out-of-plane displacement which is easily measurable. Our previous study experimentally proved that clearer images can be obtained using the diffuse field concept in which chirp waves are exited instead of burst waves[15]. However, it only indicated the superiority of the use of a wider frequency range for the imaging and did not discuss an appropriate frequency range. From the above, this paper discusses the effect of frequency ranges on images of delamination in the SLS imaging using the diffuse field concept. In Sect. 3, vibration in a metal block by external forces is formulated with finite element method, considering an aluminum alloy block used in the later experiment. In Sect. 4, resonances and the SLS imaging are discussed for an intact specimen and a specimen with an artificial delamination. Based on the above results, nondestructive evaluation (NDE) using the SLS technique for small defects of the order of micrometer is discussed in Sect. 4.5.

3. Formulization of resonance with finite element method

In this section, vibrations of a metal block by external forces are formulated and discussed with finite element method and the resonant frequencies and their vibration patterns are calculated.

Considering the harmonic vibration of an angular frequency ω, the equation of motion in a linear elastic body is written in frequency domain as,

$$(\boldsymbol{K} - \omega^2 \boldsymbol{M})\boldsymbol{U} = \boldsymbol{F} \ , \tag{1}$$

where $\boldsymbol{K}$ and $\boldsymbol{M}$ are stiffness and mass matrices respectively, which are determined by known parameters such as elastic constant, mass density, and configuration of an elastic object. $\boldsymbol{U}$ is a vector that consists of the displacements at all nodal points of finite element method and $\boldsymbol{F}$

is a force vector expressed as external concentrated loadings on all nodal points. Let the number of the elements in U be M, F is also the vector with the order of M, and K and M are the $M{\times}M$ square matrices. Because K and M are positive semidefinite symmetric matrices, the eigenvalues ω_m^2 in Eq. (1) with $F{=}0$ are real numbers greater than or equal to 0 ($m{=}1, 2, \ldots, M$). Since the eigenvectors $\boldsymbol{\varphi}_m$ are orthogonal to each other, U can be expressed as a linear combination of $\boldsymbol{\varphi}_m$ as follows.

$$U = \sum_{m=1}^{M} \alpha_m \boldsymbol{\varphi}_m \ . \tag{2}$$

The scalar coefficient α_n can be written as the following Eq. (3) by substituting Eq. (2) to Eq. (1) and then multiplying $\boldsymbol{\varphi}_n^T$ from the left of both sides.

$$\alpha_n = \frac{\boldsymbol{\varphi}_n^T F}{\boldsymbol{\varphi}_n^T (K - \omega^2 M)\boldsymbol{\varphi}_n} \ . \tag{3}$$

Applying $(K - \omega_n^2 M)\boldsymbol{\varphi}_n = 0$ to Eq. (3), α_n is rewritten as

$$\alpha_n = \frac{\boldsymbol{\varphi}_n^T F}{(\omega_n^2 - \omega^2)\boldsymbol{\varphi}_n^T M \boldsymbol{\varphi}_n} \ . \tag{4}$$

Therefore, given external forces F, the nodal displacement vector U is

$$U = \sum_{m=1}^{M} \frac{\boldsymbol{\varphi}_m^T F}{(\omega_m^2 - \omega^2)\boldsymbol{\varphi}_m^T M \boldsymbol{\varphi}_m} \boldsymbol{\varphi}_m \ . \tag{5}$$

Given external forces are $g(t)$ in time domain, the nodal force vector F can be expressed in the frequency domain as,

$$F = F_0 G(\omega), \tag{6}$$

where $G(\omega)$ is the Fourier transform of $g(t)$, and F_0 is a constant vector consisting of non-zero values at nodes that the external force is applied to. The nodal displacement vector in the time domain is

$$\boldsymbol{u}(t) = \int_{-\infty}^{\infty} U \exp(-i\omega t)\, d\omega$$

$$= \sum_{m=1}^{M} \int_{-\infty}^{\infty} \frac{\boldsymbol{\varphi}_m^T F_0 G(\omega)}{(\omega_m^2 - \omega^2)\boldsymbol{\varphi}_m^T M \boldsymbol{\varphi}_m} \boldsymbol{\varphi}_m \exp(-i\omega t)\, d\omega \ . \tag{7}$$

If the external forces are the harmonic wave with an angular frequency of ω_0, $g(t)$ is expressed as $G(\omega) = \delta(\omega - \omega_0)$ in the frequency domain. Then, Eq. (5) becomes

$$U = \sum_{m=1}^{M} \frac{\boldsymbol{\varphi}_m^T \boldsymbol{F_0}}{(\omega_m^2 - \omega^2)\boldsymbol{\varphi}_m^T \boldsymbol{M}\boldsymbol{\varphi}_m} \boldsymbol{\varphi}_m \, \delta(\omega - \omega_0) \quad . \tag{8}$$

Therefore the nodal displacement vector in the time domain is

$$\boldsymbol{u}(t) = \int_{-\infty}^{\infty} \boldsymbol{U} \exp(-i\omega t) \, d\omega$$

$$= \sum_{m=1}^{M} \frac{\boldsymbol{\varphi}_m^T \boldsymbol{F_0}}{(\omega_m^2 - \omega_0^2)\boldsymbol{\varphi}_m^T \boldsymbol{M}\boldsymbol{\varphi}_m} \boldsymbol{\varphi}_m \exp(-i\omega_0 t) \quad . \tag{9}$$

Considering excitation by laser irradiation, narrowband waves with the angular frequency of ω_0 can be excited by modulating continuous waves of laser. If ω_0 takes the value close to a resonant angular frequency ω_m, the resonant mode is largely generated due to the effect of $1/(\omega_m^2 - \omega_0^2)$ in Eq. (9).

When the external loading is expressed as a continuous function, Eq. (7) is written as follows by applying path integration and residue theorem to infinite integration.

$$\boldsymbol{u}(t) = \pi i \sum_{m=1}^{M} \frac{\boldsymbol{\varphi}_m^T \boldsymbol{F_0} G(\omega_m)}{\omega_m \boldsymbol{\varphi}_m^T \boldsymbol{M}\boldsymbol{\varphi}_m} \boldsymbol{\varphi}_m \exp(-i\omega_m t) \quad . \tag{10}$$

Now considering the external loading is ranging from ω_{min} to ω_{max}, the summation in Eq. (10) is limited in the frequency range and can be written as,

$$\boldsymbol{u}(t)$$

$$= \pi i \sum_{\substack{m=1 \\ \omega_{min} < \omega_m < \omega_{max}}}^{M} \frac{\boldsymbol{\varphi}_m^T \boldsymbol{F_0} G(\omega_m)}{\omega_m \boldsymbol{\varphi}_m^T \boldsymbol{M}\boldsymbol{\varphi}_m} \boldsymbol{\varphi}_m \exp(-i\omega_m t) \quad . \tag{11}$$

In elastic wave generation by laser, broadband vibration can be established using pulsed laser irradiation. Then, because the frequency range in Eq. (11) becomes broad, Eq. (11) is given as the sum of wave fields with many resonant modes. Thus, a certain resonant mode does not remarkably appear unlike applying harmonic wave.

Equations (9) and (11) show the displacement distribution $\boldsymbol{u}$ for a certain external loading at a specific source location $\boldsymbol{F_0}$. This means that the equations show waveforms received at the nodal points of a whole structure when elastic waves are excited at a fixed position by laser. Considering reciprocal theorem in which the same waveforms can be received even if the positions of excitation and reception exchange, the distribution of the displacements by excitation at a fixed position is equivalent to that of the waveforms excited

at the multiple positions by scanning a laser spot. Therefore, Eqs. (9) and (11) correspond to the distribution of the multiple waveforms obtained with the SLS technique.

4. Results and discussions

4.1 Resonant frequencies and wave structures

First of all, resonant frequencies and wave structures of low order modes were calculated for a rectangular parallelepiped aluminum alloy block of $50 \times 80 \times 21$ mm^3 with finite element method described in Sect. 3, where the elastic block was discretized into 10, 20, and 7 elements respectively and had the longitudinal velocity of 6300 m/s and the transverse velocity of 3100 m/s. The lowest 25 resonant frequencies $f_m (= \omega_m/2\pi$) were provided as 0.0, 0.0, 0.0, 0.0, 0.0, 0.0, 12.8, 14.3, 22.7, 25.9, 30.8, 31.0, 31.3, 31.9, 37.1, 40.5, 44.3, 45.0, 46.2, 47.2, 48.8, 49.5, 52.5, 53.0, 54.9 kHz. The first six eigenvalues of 0 indicate the translational and rotational motion of a rigid body with respect to the three Gaussian axes, which are now negligible because they cannot be measured by a vibrometer. Figure 2 shows the distributions of the absolute values of the out-of-plane displacement on the surface of 50×80 mm^2 at four selected resonant frequencies. The dark areas show the anti-nodes with great amplitude and the bright areas are the nodes. The distributions differ in the resonant frequencies and agree well with the experimental results shown later.

4.2 Experimental results of resonance frequencies and wave structures

In this section, resonant frequencies and wave structures are experimentally measured with SLS for a rectangular parallelepiped aluminum alloy block (A5052) of $50 \times 80 \times 21$ mm^3. Figure 3 illustrates the experimental set-up. A digital-to-analogue converter (NI, USB-6364, 16-bit) generates modulated signals and a fiber laser (SPI Laser, G4 50W-S-HS) receives the modulated signals and emits modulated laser beam to a Galvano mirror scanner that allows a laser spot to be scanned two-dimensionally. The out-of-plane vibrations are detected at a fixed position with a laser Doppler vibrometer (LDV) (Polytec, OFV-5000) after propagating and reflecting within the structure and the waveforms are transmitted to a personal computer as digitalized data for analysis. In the following experiments, the waveforms are obtained through the high pass filter of 0.1 kHz and the low pass filter of 100 kHz built in the LDV.

First, resonant frequencies are experimentally measured for three different positions of a laser source. Considering the coordinates whose origin locates at the center of the block surface as shown in Fig. 4, elastic waves were generated at (x, y)=(0 mm, 0 mm), (0 mm, 20 mm), and (-35 mm, -20 mm) which were selected to measure many resonant modes with different anti-nodes. The out-of-plane vibrations were measured at (x, y)=(35 mm, 0 mm). Narrowband burst waves were excited by laser irradiation modulated for the duration of 10 ms and the waveforms were recorded within 20 ms from the beginning of the laser irradiation after averaging 5 signals. Figures 5(a) and 5(b) show a typical waveform and its frequency spectrum at the modulation frequency of 14.3 kHz that is one of the resonant frequencies in the specimen. A narrowband waveform is shown in Fig. 5(a) and there exists a sharp spectrum peak at 14.3 kHz in 5(b). Next, the frequency spectrum is created by plotting the maximum values of the frequency spectrum obtained at 41 modulation frequencies from 10 kHz to 50 kHz at 0.1 kHz increment. Figures 6(a), 6(b), and 6(c) show the frequency spectra for the source positions of (x,y)=(0 mm, 0 mm), (0 mm, 20 mm), and (-35 mm, -20 mm), respectively. The dashed lines in Fig. 6 denote the resonant frequencies f_m calculated in Sect. 4.1. Although the frequencies of the spectrum peaks in Fig. 6 vary with the positions of the laser source, all the frequencies agree well with the resonant frequencies calculated. This indicates that the resonant modes do not largely measured if the exciting or receiving position locates at a node of the modes.

Next, distributions of out-of-plane vibration were experimentally obtained with the SLS at the resonant frequencies shown in the calculation results of Fig. 2. The distributions were created by plotting the maximum values of the frequency spectrum measured at 1 mm increments in the dashed-line area of 66 × 40 mm^2 as shown in Fig. 4. Figure 7 shows the experimental distributions agree well with the resonant patterns derived by the calculations shown in Fig. 2 even though the exciting source and the receiving position are interchanged.

4.3 Resonant frequencies in the specimen with a delamination

In this section, the resonant frequencies of the specimen with an artificial cylindrical delamination are measured in a similar way to that in Fig. 6. The specimen with an artificial delamination consists of an aluminum alloy plate (A5052) of 50 ×80 ×1 mm^3 and a rectangular aluminum alloy block (A5052) of 50 ×80 ×20 mm^3 with a cylindrical dent 10

mm in diameter and 0.05 mm in depth on the surface, and both of them are attached with adhesives (cyanocrylate glue produced by TOAGOSEI) as shown in Fig. 8. As a result, the dent can be regarded as an artificial delamination. Although the authors have been studied SLS imaging for defects in plate-like structures, subsurface delamination in an aluminum block shown in Fig. 8 is used in this experiment for future application to small objects as written in Sect. 4.5. In addition to such small objects, applications to inspection for disband of aircrafts and automobiles and for small inclusion near the surface of aluminum alloy materials are also considered.

Figure 9 shows the frequency spectra for different laser sources at $(x,y)=(0$ mm,0 mm), $(0$ mm,20 mm), and $(-35$ mm,-20 mm) on the surface of the specimen with the artificial delamination measured in the same way as in Fig. 6. The upper dashed lines show the values for the intact specimen shown in Fig. 6 and the lower solid lines show those for the specimen with the artificial delamination. The peak values of the both lines appear at the same frequencies, which reveal that the resonant frequencies of the whole structure do not change whether there exists the small delamination or not.

This is because the local resonant frequencies at the delamination are largely different from the frequency range measured in the experiments. The local defect resonance (LDR) is induced at a cylindrical defect and many papers on the inspection using the LDR have been published as in Refs. 21) and 22). In the case of a cylindrical defect, the fundamental LDR frequency is expressed as follows,

$$f_{\mathrm{LDR}} = \frac{1.6h}{a^2} \sqrt{\frac{c_T^2(3c_L^2 - 4c_T^2)}{9(c_L^2 - c_T^2)}}, \qquad (12)$$

where h, a, c_L and c_T are the distance from surface to the defect, the radius of the defect and the longitudinal and transverse velocity of the material, respectively. In the case of the specimen used in the experiment, the fundamental LDR frequency is 108 kHz which is beyond the frequency range measured in the experiment. In Refs. 21) and 22), cylindrical delamination was detected using an LDR frequency, and so the inspection using LDR is effective for NDT when the LDR frequency is in the range of measurable frequency. However, measurable frequency range is generally smaller than LDR frequency for inspection of small defects. In addition, because LDR frequency severely depends on the size and configuration of defects, images for defects cannot be stably obtained that is the

critical problem for NDT. Therefore, this study discusses the effectiveness of SLS imaging in the lower frequency range than the LDR frequency.

4.4 SLS images for a cylindrical delamination

Images for the specimen with the artificial delamination are obtained through the SLS imaging in this section. The laser spot for wave excitation with the diameter of 5 mm was scanned over the area surrounded by the dashed line of 20 ×20 mm^2 at 1 mm increment as shown in Fig. 8. The duration of laser emission was 10 ms and the waveforms were recorded for 20 ms from the beginning of the excitation at all laser source positions. First, in order to study how the resonance affects the SLS imaging, narrowband burst waves were used as modulation signals, and the vibration distributions were obtained in grayscale by plotting the spectrum peak values at all laser source positions. Figures 10 (a) – 10 (d) show the vibration distributions at four resonant frequencies of 14.3, 25.9, 31.0, and 46.2 kHz as used in Figs. 2 and 7. In Figs. 10 (a) and 10(d), the delamination clearly appears because an antinode of the resonance mode is located at the demalination area. On the other hand, the delamination cannot be found in Figs. 10(b) and 10(c) because the antinodes of the resonance locate out of the delamination area. Namely, detectability of the delamination strongly depends on the frequency of the burst wave. The use of narrowband burst wave disturbs generation of diffuse fields and the image significantly includes resonance patterns as well as defect images.

Next, broadband chirp waves were used as modulation signals to obtain images. Although a broadband pulse wave can be used to establish diffuse fields in Refs. 19) and 20), chirp waves modulated in long time are adopted to measure signals with high signal-to-noise ratio (SNR). The waveforms were received after averaging five signals at each point to enhance SNR, and the vibration distributions were created with a grayscale by plotting values that were integrated the square of spectrum within the frequency range used for excitation[11]. When diffuse fields are used, the waveforms recorded before diffuse fields are established should not be applied to imaging. However the coherent fields in the early waveforms does not affect images very much because we can estimate that it takes less than 1 ms to establish diffuse fields from the size and velocity of the specimen used in this experiment. First, a chirp signal in the frequency range of (a) 1-10 kHz, which does not

include resonant frequencies of the whole structure, was used. Then the frequency range of the modulation chirp signals were set to (b) 10-20 kHz, (c) 10-30 kHz, (d) 10-40 kHz, (e) 10-50 kHz, and (f) 10-100 kHz. Figures 11(a) − 11(f) show the images obtained using the frequency ranges, respectively. The delamination does not appear in Fig. 11(a) using the frequency range smaller than the fundamental resonant frequency because the frequency range $\omega_{min} - \omega_{max}$ in Eq. (11) does not include the resonant frequencies and Eq. (11) becomes 0. The delamination images become clearer as the frequency range becomes broader above the fundamental resonant frequency. This is because the number of the resonant modes included in the summation in Eq. (11) increases as the frequency range becomes broader, and therefore the broadband waves establish diffuse fields and the effect of resonant patterns become reduced, and as a result the delamination clearly appears in the images. The white part of the boundary of delamination is due to evanescent modes that appear when waves are excited near boundaries, and this effect agrees well with the result from the calculation in Ref. 12).

Based on these results, it is concluded as follows. Clear images of defects cannot be obtained due to low SNR when using the frequency range below the fundamental resonant frequency (Fig. 11(a)). However if the frequency range include resonant frequencies SNR improves and, both the resonant patterns and the variation of local bending stiffness can appear in images (Fig. 10). Therefore, if waves with wide frequency range like chirp waves including multiple resonant frequencies are used to establish diffuse fields, then clear images can be obtained in which only delamination appears without the resonant patterns.

4.5 Detectability of submillimeter defects

The SLS imaging for defects using the diffuse field concept can be applied to complex and small structures in which there exist many reflected waves as described in Sect. 1 and Sect. 2. This means that we can use the measurable frequency range of the order of MHz even for the inspection of micro defects.

Submillimeter defects generated inside such small industrial products as integrated circuits (IC), micro electro mechanical systems (MEMS) and bonded interfaces between their basis and silicon wafer may cause serious problem like deterioration of strength. Therefore the inspection of such defects is needed through the productive process. In

addition, carbon fiber reinforced plastics (CFRP), which have been widely used in aircrafts and space crafts, require periodic inspection and evaluation because failure may start from voids and delamination smaller than a millimeter located at interfaces of the layers, which often leads catastrophic destruction of the entire structure. Therefore NDT for such micro defects are studied[23),24)].

In Sect. 4.4, it was confirmed that the frequency range below 20 kHz or 100 kHz can be applied to the SLS imaging for delamination 10 mm in diameter and 1 mm in deep. Based on these results, we can estimate that the measurable frequency range of the order below 20 MHz is available to detection of delaminations and inclusions of the order of 10 μm. Ultrasonic measurements using the frequency range of the order below 20 MHz has been widely used in the conventional ultrasonic NDT and a large number of measurement devices such as transducers and amplifiers can be found. Therefore the SLS imaging using the diffuse field concept in the low frequency range can be effectively applied to submillimeter defects.

5. Conclusions

In imaging inspection of delamination using the SLS technique, the effect of the frequency ranges used for imaging was discussed with FEM and experiments. First, it was described that the displacements distributions in a metal block depend on frequencies with the formulation of FEM and it was confirmed that the resonant frequencies and the resonant patterns calculated with FEM agree well with the experimental results using the SLS imaging. Next, defect images were experimentally obtained through the SLS imaging in which narrowband burst waves and broadband chirp waves were used in order to discuss the frequency dependence on defect images. The use of narrowband burst waves is inappropriate for defect images because diffuse fields were not established and the effect of the resonances depending on the frequency appeared in the images. On the other hand, in the case of broadband chirp waves, images for delamination cannot be obtained when the frequency ranges below the fundamental resonant frequency are applied, and clearer images can be obtained as the frequency range becomes broad above the fundamental resonant frequency. Because the SLS imaging with frequency ranges around 10-30 kHz or so enabled us to obtain images for delamination 10 mm in diameter, non-contact imaging inspection for

a defect of the order of submillimeter can be realized by applying measurable frequencies with conventional devices that have been widely used in ultrasonic NDE.

Acknowledgement

References

1) S. J. Davies, C. Edwards, G. S. Taylor, and S. B. Palmer, J. Phys. D: Appl. Phys. 26, 329 (1993).

2) A. Harata, and T. Sawada, Jpn. J. Appl. Phys. 32, 2188 (1993).

3) H. Nakaono, and S. Nagai, Jpn. J. Appl. Phys. 32, 2540 (1993).

4) J. D. Achenbach, J. Mech. Phys. Solid 51, 1885 (2003).

5) I. A. Veres, T. Berer, and P. Burgholzer: Ultrasonics 53, 141 (2013).

6) W. Liu, and J. W. Hong, Ultrasonics 55, 113 (2015).

7) J. Wang, and Q. Feng, Jpn. J. Appl. Phys. 54, 046602 (2015).

8) C. B. Scruby, and L. E. Drain, Laser ultrasonics: techniques and applications (CRC Press, Bristol, 1990).

9) T. Hayashi, Int. J. Press. Vessels Pip. 153, 26 (2017).

10) T. Hayashi and K. Ishihara, Ultrasonics 77, 47 (2017).

11) A. Maeda, and T. Hayashi, Mater. Trans. 59, 320 (2018).

12) T. Hayashi, and S. Nakao, Mater. Trans. 58, 1264 (2017).

13) S. Nakao, and T. Hayashi, J. Nondestruct. Eval. Diagnostics Progn. Eng. Syst. 1 (2018).

14) T. Hayashi, J. Acoust. Soc. Am. 143 EL 260 (2018).

15) T. Hayashi, Appl. Phys. Lett. 108, 081901 (2016).

16) S. Nakao and T. Hayashi, Proc. 39th Symp. Ultrasonic Electronics, 2018, 3P2-3.

17) A. R. Clough, and R. S. Edwards, NDT&E Int. 62, 99 (2014).

18) A. R. Clough, and R. S. Edwards, Ultrasonics 59, 64 (2015).

19) M. J. Evans and P. Cawley, J. Acoust. Soc. Am. 106, 3348 (1999).

20) R. L. Weaver, J. Sound and Vib. 94, 319 (1984).

21) F. Ciampa, G. Scarselli, and M. Meo, J. Acoust. Soc. Am. 141, 2364 (2017).

22) J. Hettler, M. Tabatabaeipour, S. Delrue, and K. V. D. Abeele, J. Nondestruct. Eval. 36:2 (2017)

23) H.Sato, S. Nakano, H. Ogiso, and K. Yamanaka, Jpn. J. Appl. Phys. 36, 3267 (1997).

24) T. Tanaka and Y. Izawa, Jpn. J. Appl. Phys. 40, 1477 (2001).

Figure Captions

Fig. 1. Amplitude variation of the received signals with the position of a laser source in SLS technique.

Fig. 2. Resonant patterns obtained with finite element calculations.

Fig. 3. Schematic illustration of the experimental set-up.

Fig. 4. Defect-free specimen and source and receiving positions.

Fig. 5. A typical waveform at 14.3 kHz and its frequency spectrum.

Fig. 6. Frequency spectrum for the laser sources at different positions: (a) (0,0), (b) (0,20), and (c) (-35,-20). The dashed lines are the resonant frequencies obtained with the calculation in Sect. 3.

Fig. 7. Resonant patterns experimentally obtained with the SLS imaging at four different frequencies.

Fig. 8. Specimen with an artificial delamination. An aluminum alloy block with a circular dent and an aluminum thin plate were attached with adhesives.

Fig. 9. Frequency spectrum for the laser sources located at (a) (0,0), (b) (0,20), and (c) (-35,-20) (The dashed line shows the result for an intact aluminum block, and the solid line for an aluminum block with an artificial delamination).

Fig. 10. Images obtained with the SLS imaging using spectrum peak values of burst waves at the selected four frequencies.

Fig. 11. Images obtained with the SLS imaging using the integrations of the squared spectrum of chirp waves with different frequency ranges.
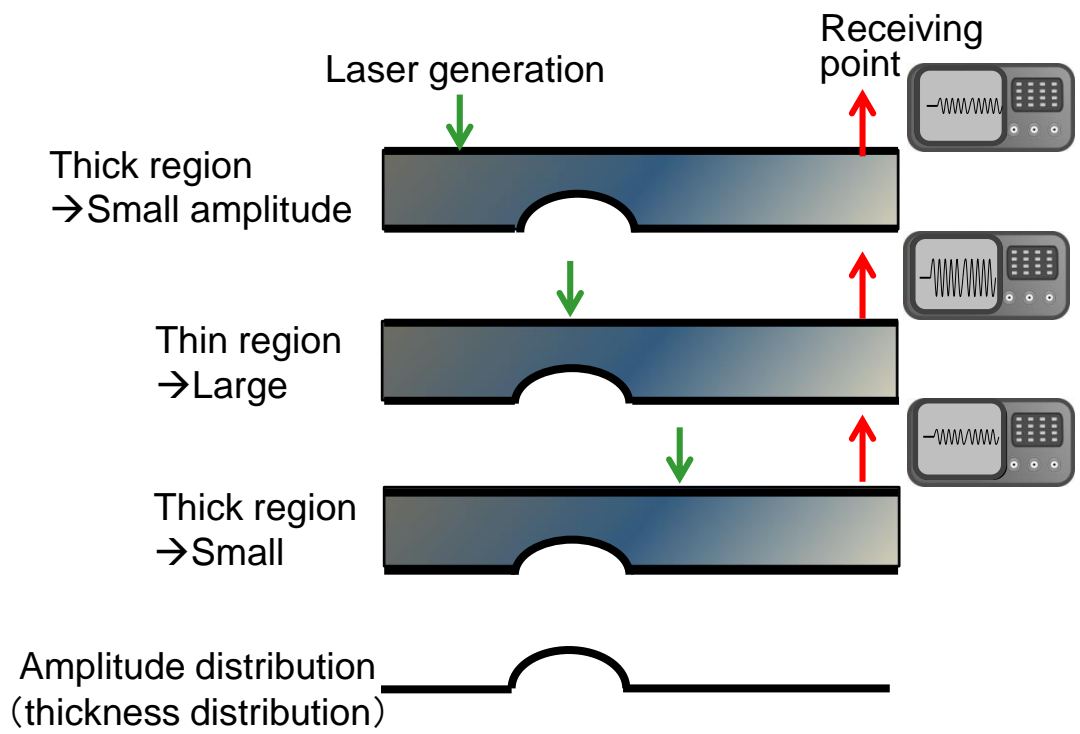
Fig.1. (Color Online)
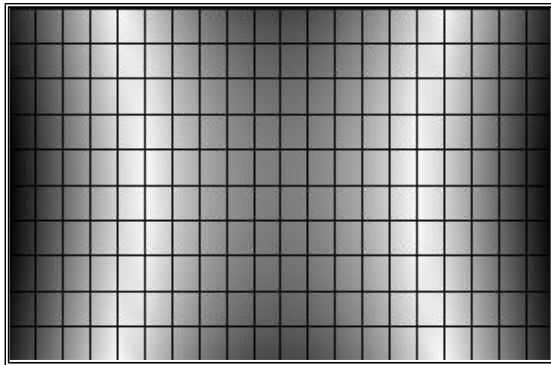
(a) 14.3 kHz
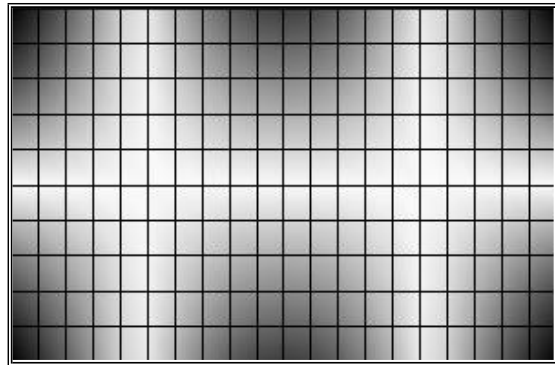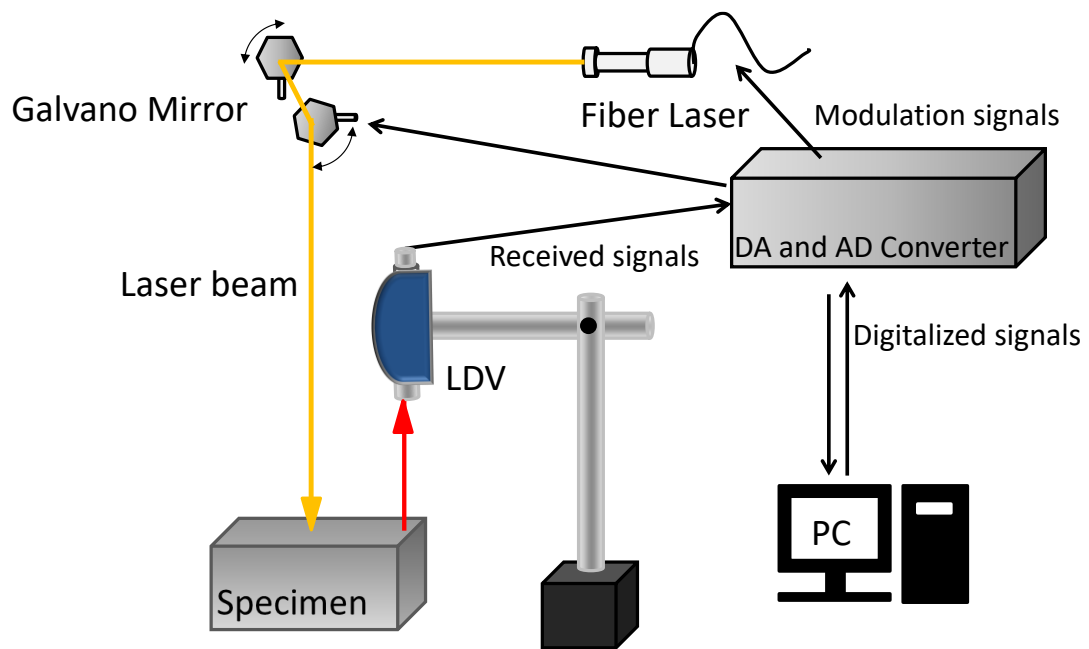
(b) 25.9 kHz
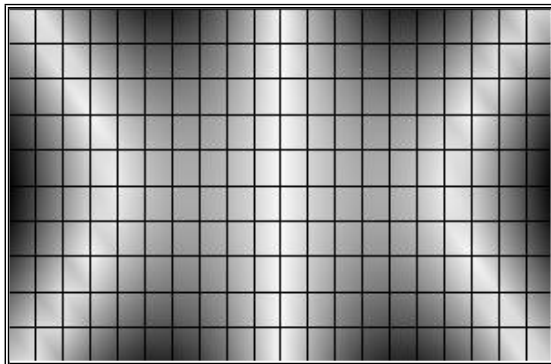
(c) 31.0 kHz
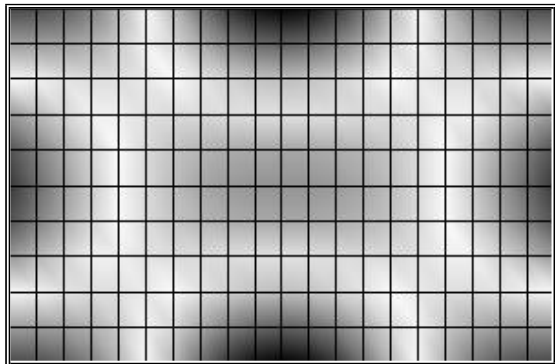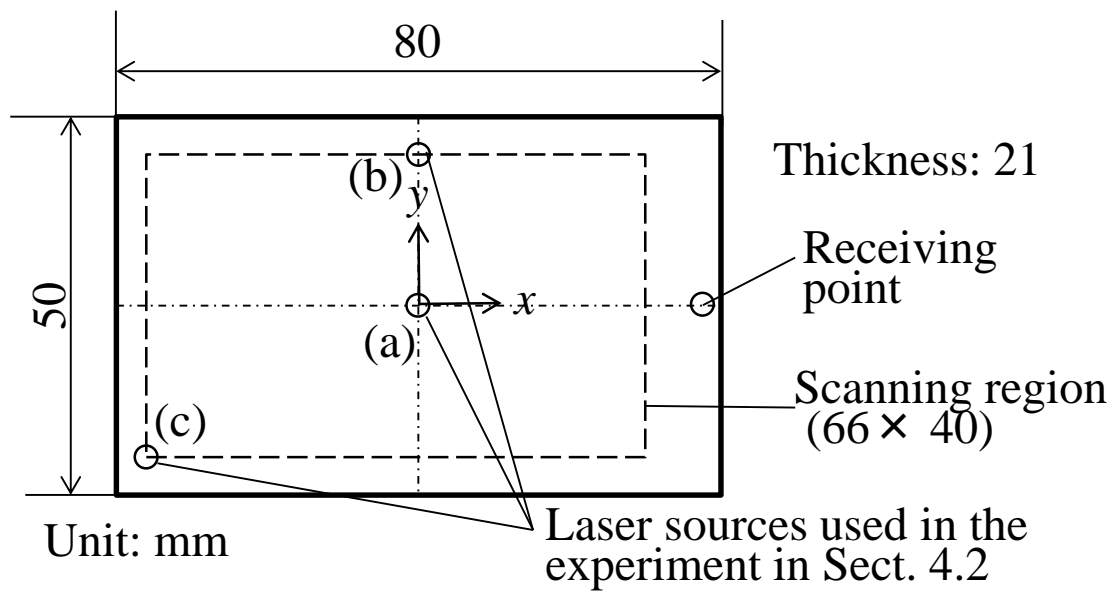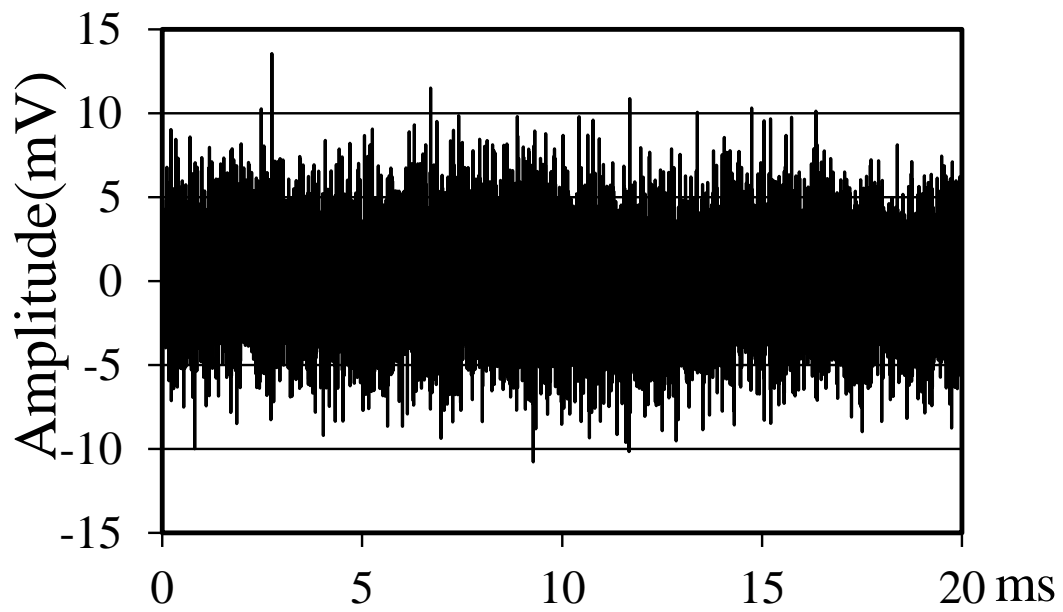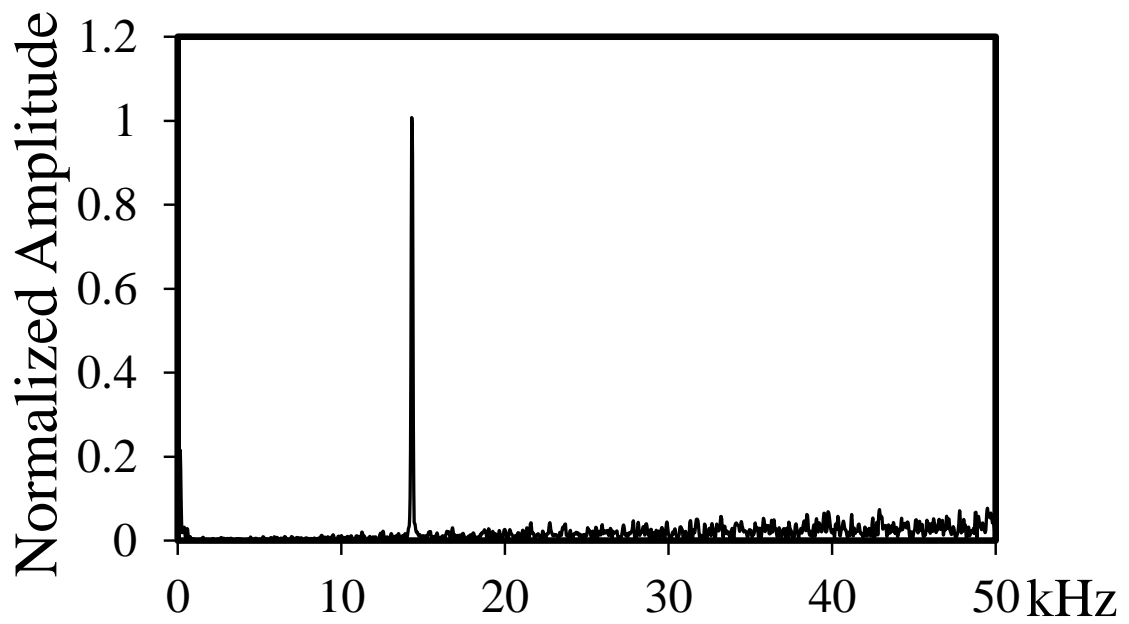
(d) 46.2 kHz

Fig. 2.

Fig. 3. (Color Online)

Fig. 4.

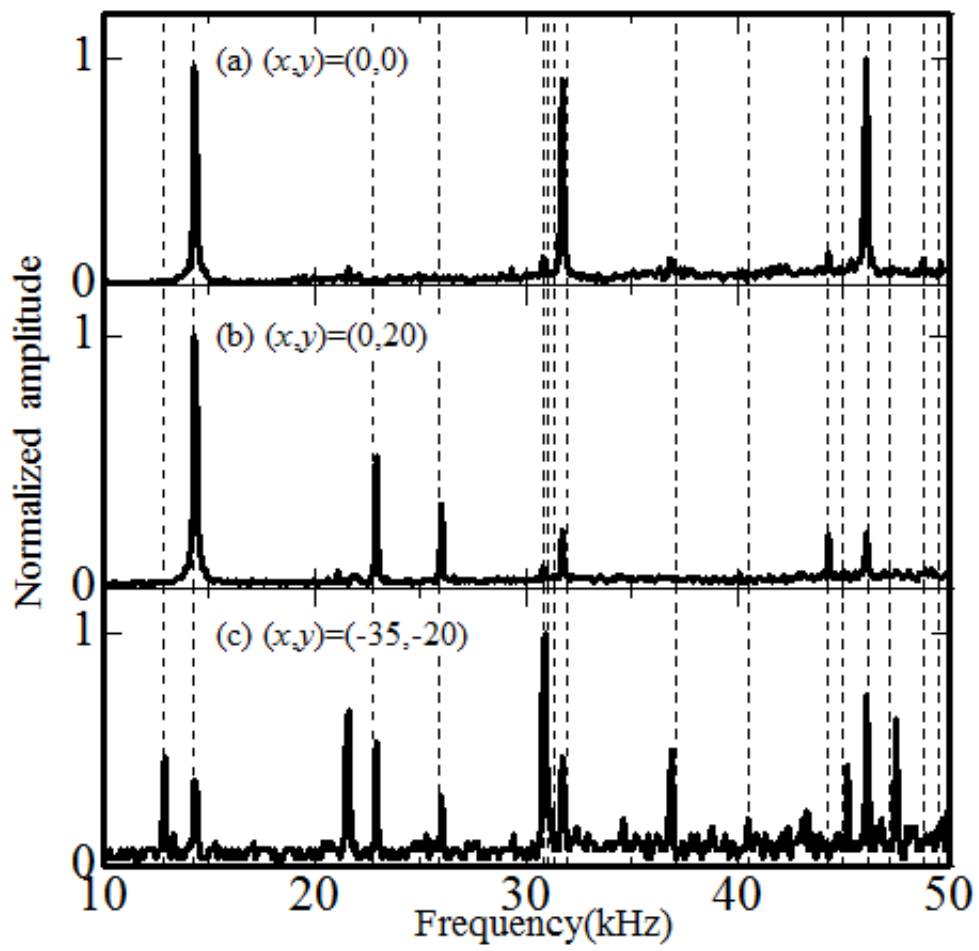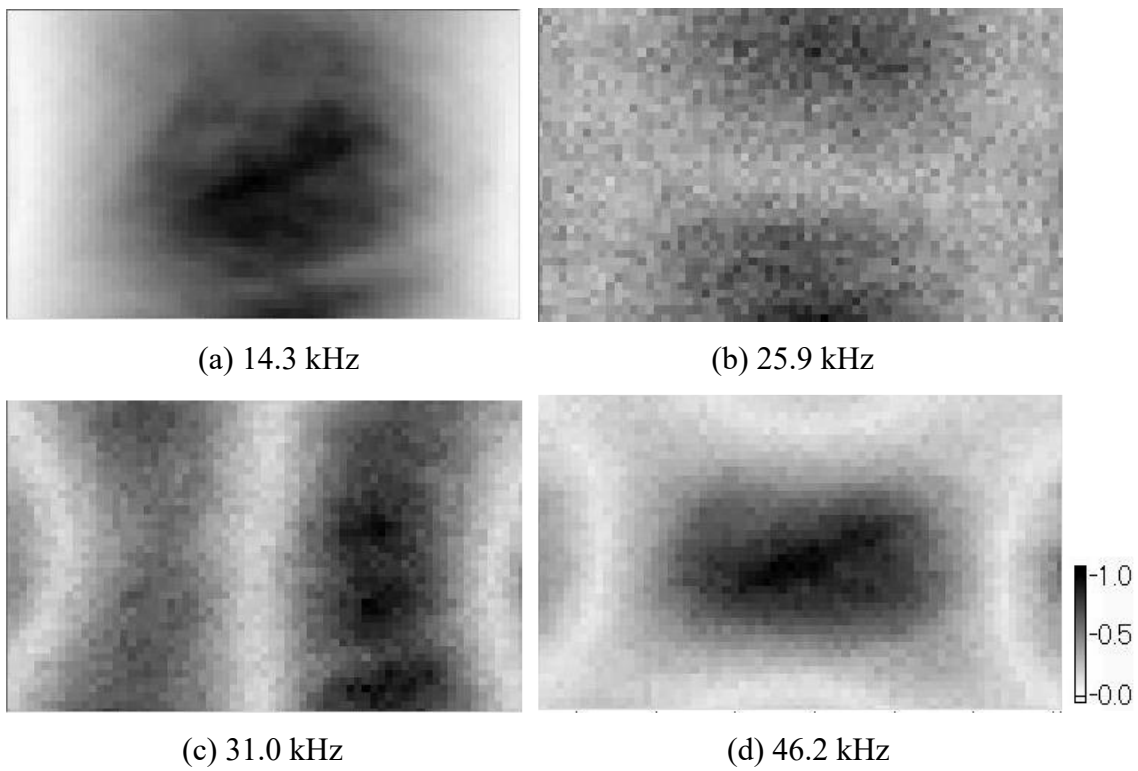(a) Typical waveform
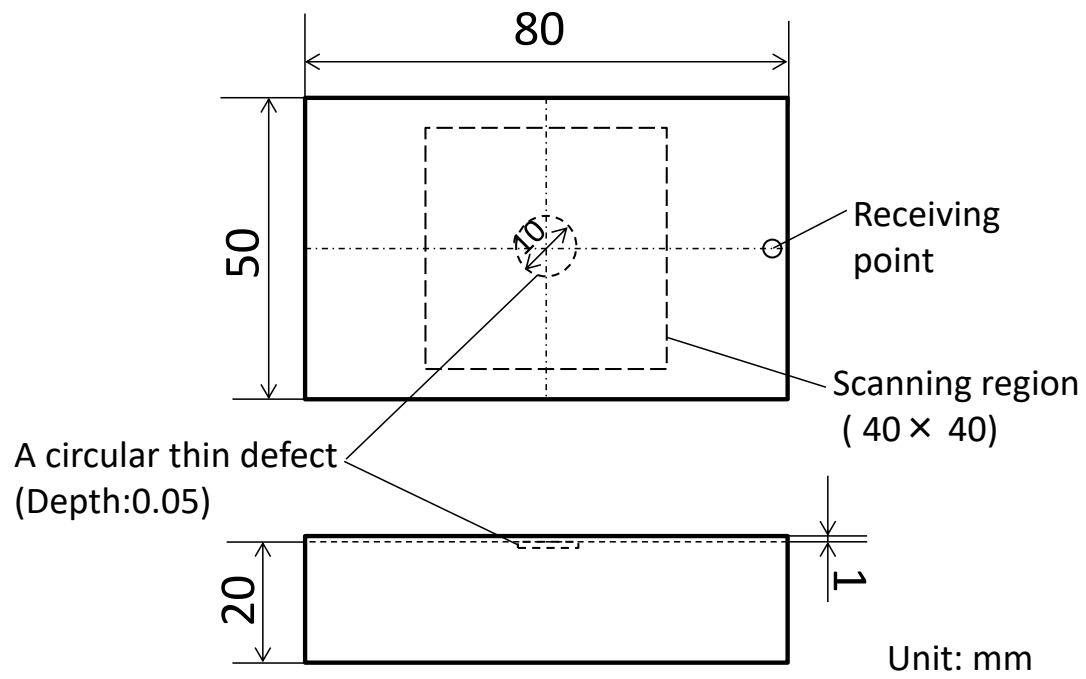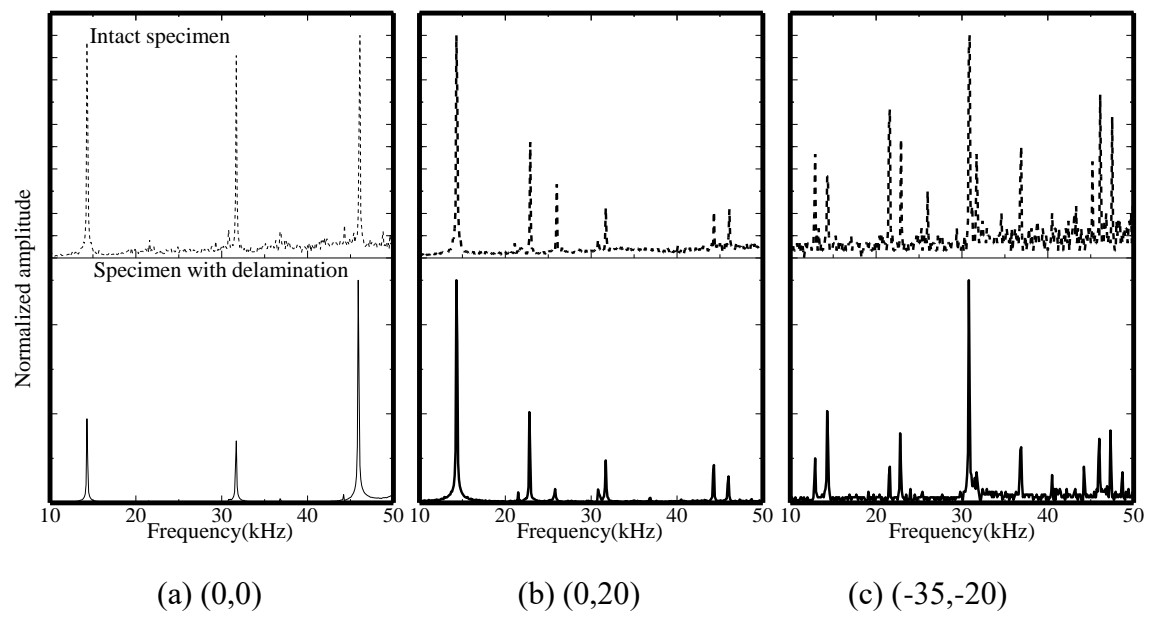

(b) Its frequency spectrum

Fig. 5.

Fig. 6.

(a) 14.3 kHz

(b) 25.9 kHz

(c) 31.0 kHz

(d) 46.2 kHz

Fig. 7.

Fig. 8.

Fig. 9.

(a) 14.3 kHz

(b) 25.9 kHz

(c) 31.0 kHz

(d) 46.2 kHz

Fig. 10.

(a) 1-10 kHz

(b) 10-20 kHz

(c) 10-30 kHz

(d) 10-40 kHz

(e) 10-50 kHz

(f) 10-100 kHz

Fig. 11.